nature communications

Article

https://doi.org/10.1038/s41467-025-60243-0

Purely electronic insulator-metal transition in rutile VO_2

Received: 29 April 2024

Accepted: 19 May 2025

Published online: 01 July 2025

Check for updates

Shaobo Cheng[1,2,9], Henry Navarro[3,4,9], Zishen Wang[5], Xing Li[1,2], Jasleen Kaur[5,6], Alexandre Pofelski[1], Qingping Meng[1], Chenyu Zhou[7], Chi Chen[5], Mark P. M. Dean[1], Mingzhao Liu[7], Ali C. Basaran[3], Marcelo Rozenberg[8], Shyue Ping Ong[5], Ivan K. Schuller[3] & Yimei Zhu[1]

Volatile resistive switching in neuromorphic computing can be tuned by external stimuli such as temperature or electric-field. However, this type of switching is generally coupled to structural changes, resulting in slower reaction speed and higher energy consumption when incorporated into an electronic device. The vanadium dioxide (VO_2), which has near room temperature metal-insulator transition (MIT), is an archetypical volatile resistive switching system. Here, we demonstrate an isostructural MIT in an ultrathin VO_2 film capped with a photoconductive cadmium sulfide (CdS) layer. Transmission electron microscopy, resistivity experiments, and first-principles calculations show that the hole carriers induced by CdS photovoltaic effect are driving the MIT in rutile VO_2. The insulating-rutile VO_2 phase has been proved and can remain stable for hours. Our finding provides a new approach to produce purely electronically driven MIT in VO_2, and widens its applications in fast-response, low-energy neuromorphic devices.

In the cognitive era, volatile and nonvolatile resistive switching has been proposed as the building block to engineer the next generation energy efficient neuromorphic computing technologies[1,2]. Among the volatile switching, metal-insulator transition (MIT) in Mott systems is particularly promising because of its low energy consumption, fast reaction speed, controllable, and repeatable behavior[3]. Most of the current methods for modulating resistive switching in MIT materials are mainly limited by heating and/or biasing, which largely restricts their applications. Furthermore, the MIT, which manifest itself in the electronic transport, is also intertwined with the structural phase transition, further limiting the switching speed[4–7]. Since metal-to-insulator and structural transitions on the same material are difficult to separate, additional functionality can be brought to a hybrid system by interfacing the MIT material with another functional material that may have high sensitivity to different external stimuli[8–12]. Therefore, it is exciting and urgent to understand and manipulate the resistive switching process in hybrid systems.

Vanadium dioxide (VO_2) is a model MIT system, with a near room-temperature transition, making it suitable for electronic device applications[13,14]. VO_2 changes from insulating monoclinic to conductive rutile phases from low temperature to high temperature. The electronic MIT is accompanied by structural transition, and monoclinic phase has dimerization of V ions along the c-axis. However, ultrafast experiments have shown that the electronic transition could be decoupled from the structural phase transition[15]. Moreover, some experiments have shown that the nonequilibrium metallic monoclinic phase can be obtained by photo-excitation, showing that isostructural MIT is possible under nonequilibrium conditions[15,16]. Recently, Lee et

[1]Department of Condensed Matter Physics and Materials Science, Brookhaven National Laboratory, Upton, NY, USA. [2]School of Physics and Microelectronics, Zhengzhou University, Zhengzhou, China. [3]Department of Physics, Center for Advanced Nanoscience, University of California San Diego, La Jolla, CA, USA. [4]Department of Physics, Andrews University, Berrien Springs, MI, USA. [5]Department of NanoEngineering, University of California San Diego, 9500 Gilman Dr, Mail Code 0448, La Jolla, CA, USA. [6]Department of Materials Science & Engineering, University of California San Diego, 9500 Gilman Dr, Mail Code 0448, La Jolla, CA, USA. [7]Center for Functional Nanomaterials, Brookhaven National Laboratory, Upton, NY, USA. [8]Laboratoire de Physique des Solides, CNRS, Université Paris Saclay, Orsay Cedex, France. [9]These authors contributed equally: Shaobo Cheng, Henry Navarro. e-mail: zhu@bnl.gov

al. successfully realized isostructural MIT in monoclinic VO_2 by electron doping[17]. Moreover, Mondal et al. used modulation doping (electron doping) to control the electronic structure of VO_2[18]. It is therefore interesting to consider the potential isostructural MIT in rutile VO_2 system, especially by doping effect.

In this work, we use a photoactive CdS layer to experimentally and theoretically explore hole doping effects on VO_2. Our results surprisingly establish a doping driven transition in VO_2, *i.e.*, creating a (meta) stable insulating rutile VO_2. This finding completes the VO_2 electronic-crystal structure phase diagram (as shown in Supplementary fig. 1). The MIT can occur entirely within the monoclinic phase and now entirely within the rutile phase. The full elucidation of the pure electronic transition would represent a major step forward in the understanding of the MIT in this important material.

Results

Basic structural characterizations and property measurement

An ultrathin 8 nm VO_2 film was epitaxially grown on a TiO_2 substrate to maximize the effect on the interfacial coupling. A CdS layer was subsequently deposited (about 80 nm thick), forming a $CdS/VO_2/TiO_2$ heterostructure. Illumination of CdS (band gap of 2.4 eV) with visible light creates photoinduced carriers[19–24] which can then drift into the VO_2 and modify its electronic properties. It is worthwhile to mention that the 80 nm CdS was chosen because this is the minimum thickness for which we can conveniently measure the electrical transport, as thinner films have too high a resistance (see Supplementary fig. 2). Figure 1A shows the schematic of experimental geometry. The samples and the Au/Pt layers were prepared using a standard focused ion beam (FIB) lift-out process[25]. The physical and structural properties were measured before and after exposure to a solar light generator. Figure 1B shows the resistance vs. temperature measurement (R-T) obtained from the cooling branch with the light on and off states. The red line is the R-T result measured before shining solar light (off state), and the black line is the result acquired after shining light (on state). The whole R-T loops and time related relaxation study results are shown in the Supplementary figs. 3–6. In the blue region, the VO_2 is insulating, while in the pink region, the VO_2 is conductive, no matter the light is on or off. However, in the yellow region (near room temperature), the VO_2 changes from insulating to metallic state when the light is turned on. Figure 1C shows a high-angle annular dark field scanning transmission electron microscopy (HAADF-STEM) image of the cross-section of the FIB sample. The energy dispersive spectrometer mapping results of the sample are shown in Supplementary fig. 7.

Since the system will relax back in 8 h after shining light (Supplementary fig. 3), systematic transmission electron microscopy (TEM) studies can be carried out to understand the mechanism of this photo-assisted MIT. For consistency, the TEM experiments (including electron diffraction and spectroscopy) were conducted within 3 h after the illumination. Figure 1D shows the selected area electron diffraction pattern acquired at room temperature at the VO_2/TiO_2 interface in $CdS/VO_2/TiO_2$ system before exposing light. Both VO_2 and TiO_2 exhibit a rutile structure, since the ultrathin VO_2 is under in-plane tensile strain from TiO_2 substrate, which is consistent with the published results[25,26]. After light exposure, yellow region in Fig. 1B, the conductivity changes dramatically (from insulating state to metallic state), while the VO_2 maintains the rutile structure as seen in Fig. 1E. This shows that the light-driven transition from insulator to metallic state is purely electronic and not driven by a structural phase transition. During the TEM observation, less than 1 nA beam current was used, which will cause less than 1 °C temperature increase[27].

Numerous studies have examined the metal–insulator transition in ultrathin VO_2 films[17,18,28–30]. The reported behavior varies significantly depending on parameters such as film thickness, substrate choice, and the presence of capping layers. While some investigations observe behavior consistent with that of bulk VO_2[18,28], others suggest that ultrathin films may undergo an isostructural MIT[17,29,30]. In this work, we investigate VO_2 films capped with CdS—a configuration that has rarely been studied. To probe possible temperature-induced structural changes, we performed X-ray diffraction (XRD) measurements above and below the transition temperature (360 K and 260 K, respectively). Clear structural changes are observed in our samples consisting of uncapped VO_2 on TiO_2 substrates (see Fig. 1F), consistent with the well-known rutile-to-monoclinic transition upon cooling[18]. In contrast, XRD data for our CdS-capped VO_2 on TiO_2 (Fig. 1G) show no detectable structural changes across the same temperature range, suggesting the

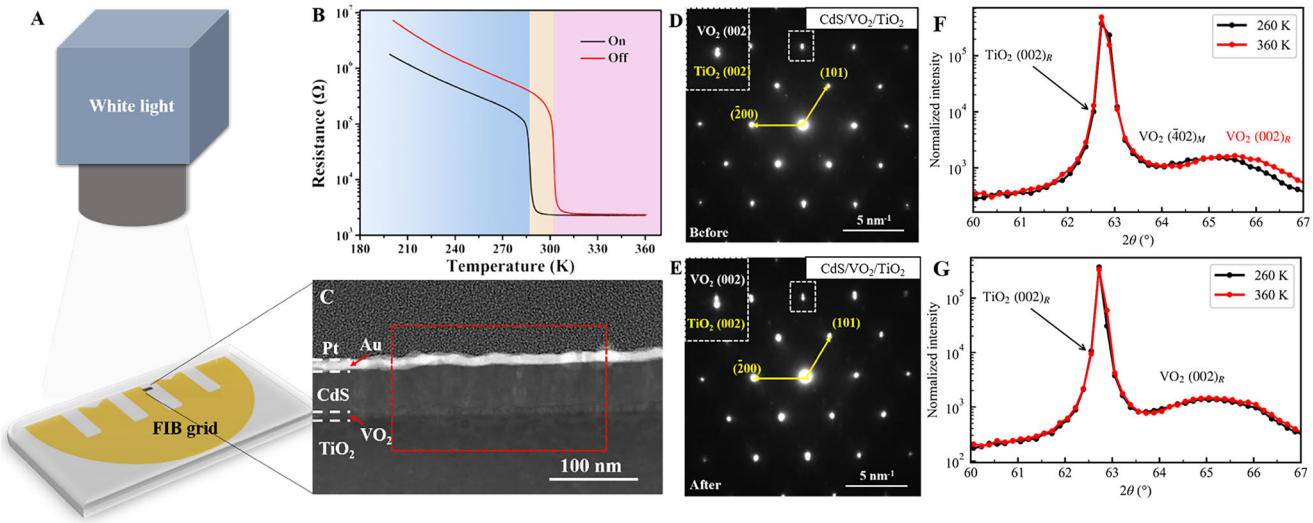

Fig. 1 | Effect of light illumination on CdS/VO_2. **A** Schematic experimental geometry. A cross-sectioned FIB (focused ion beam) sample illuminated by white light. **B** Change in the resistance across the metal-insulator phase transition measured on the cooling branch with the light ON and OFF. **C** Low magnification high angle annular dark field (HAADF) image showing the layered configuration of the sample. **D**, **E** Selected area electron diffraction patterns for the "ON" and "OFF" light states. The dashed rectangular areas are enlarged in the upper left corner of the micrograph. The TEM experiments (imaging, electron diffraction, and spectroscopy) were conducted at room temperature. Temperature dependent XRD results of (**F**) VO_2/TiO_2 system and (**G**) $CdS/VO_2/TiO_2$ system. The thickness of VO_2 film for measuring the XRD is 8 nm.

https://doi.org/10.1038/s41467-025-60243-0

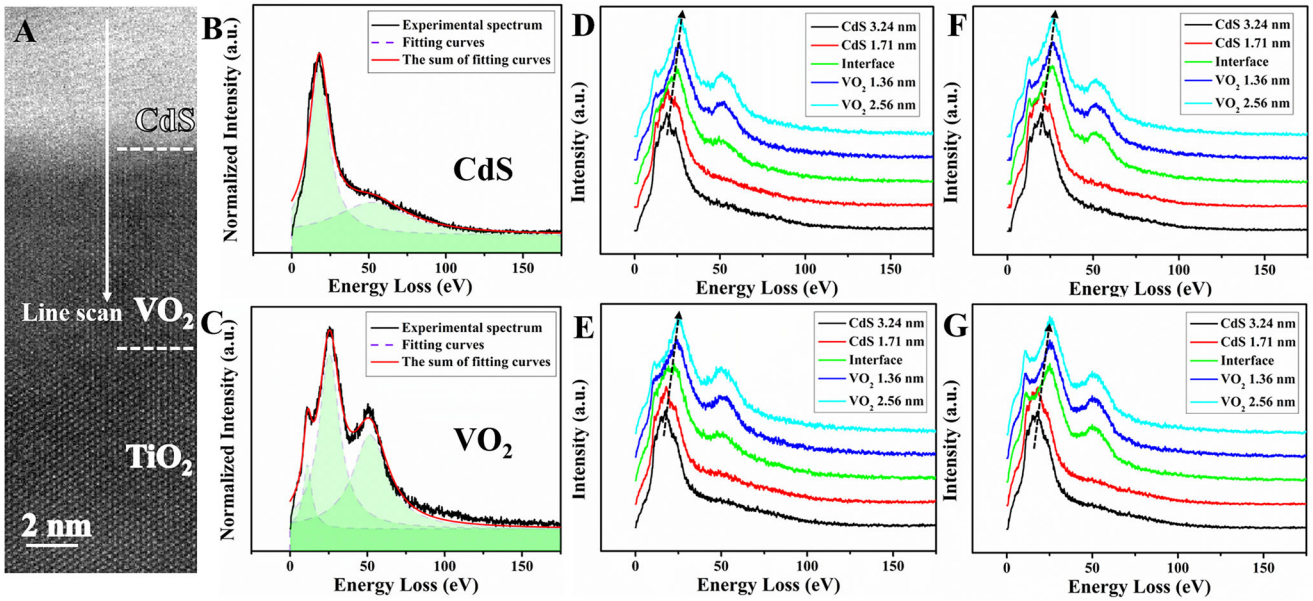

Fig. 2 | Extracted valence EELS line scans. A High-resolution HAADF-STEM image of the $CdS/VO_2/TiO_2$ interface. The white arrow indicates the EELS line scan position. Horizontal dashed lines have marked the interfaces. **B** Typical experimental EELS spectrum for CdS. Two Lorentzian functions were used to fit the spectrum. **C** Experimental EELS spectrum for VO_2. Three peaks were fitted. EELS spectra were measured at different positions from the CdS/VO_2 interface with light OFF (**D**) and ON (**E**). (**F**, **G**) are the calculated EELS spectra using the experimentally extracted dielectric function from (**D**, **E**), respectively. The black arrows show the blue shift of the spectra across the interface from CdS to VO_2.

absence of a structural transition. Given that electron diffraction confirms the rutile structure at room temperature (see Fig. 1D), we attribute the observed MIT in the capped films to a rutile-to-rutile transition, consistent with an isostructural mechanism.

Electron energy loss spectroscopy results

Electron energy loss spectroscopy (EELS) in TEM has been widely applied to study the electronic structure of materials. The signal of valence EELS (low-loss part of the spectrum) is two orders of magnitude stronger than the core-loss part. The dominant feature of valence EELS is from collective excitations (plasmons). The position of the plasma peak (the highest peak) is related to the density of valence electrons (and their effective mass)[31–33]. Thus, the peak position change reflects the evolution of valence electrons (the details can be found in the Supplementary Information).

Figure 2A is a typical HAADF-STEM image showing the $CdS/VO_2/TiO_2$ structure. EELS line scan was taken across CdS/VO_2 interface (the white arrow area). Figure 2B, C show the reference valence EELS spectra of CdS and VO_2 acquired from the regions far from the interface, respectively. To retrieve plasma components from these valence EELS, multiple Lorentzian functions have been used to fit every valence EELS spectrum[33–35]. The position of the plasma peak is determined from the fitting (as shown in Fig. 2A, B). Two peaks were identified for CdS, and three peaks were fitted for VO_2. Figure 2D shows typical extracted valence EELS spectra from different positions before light exposure, *i.e.*, the black line is the valence EELS acquired in CdS (3.24 nm from the CdS/VO_2 interface). The extracted valence EELS spectra after light exposure are shown in Fig. 2E.

The valence EELS in an inhomogeneous medium reflects the electron state at the measured point and the dielectric coupling between the measured point and nearby areas. The dielectric coupling in valence EELS has been considered based on the dielectric function theory[36–38]. Figure 2F, G are calculated valence EELS spectra by using the dielectric functions retrieved from the experiments (see Supplementary Information), which share similarities to the experimental spectra in Fig. 2D, E, respectively[36]. The current dielectric function theory[36–38] assumes that the materials at the two sides of the interface are homogeneous, and their dielectric functions have step changes across the interface. However, this ideal case may not represent experimentally obtained interfaces and the homogeneity near the interface may be destroyed by interfacial strain[39–42], atomic rearrangement, charge transfer, etc.[43,44]. So, the deviation between calculated and experimental EELS mainly comes from aforementioned inhomogeneous structure near the interface.

The plasma peak dominates the valence EELS, and the position of the plasma peak relates to the density of valence electrons (the details can be found in Supplementary Information):

$$E = \hbar\omega_P = \hbar\sqrt{\frac{4\pi e^2 N_V}{m}} \quad (1)$$

where E is the energy loss of plasma peak (*i.e.* the highest plasma peak position in EELS), N_v is the density of the valence electrons, ω_P is the plasmon frequency, e and m are electron charge and mass[33]. The shift of plasma peak is related to the change of the density of the valence electrons.

Figure 3A, B show the energy of the plasma peak as a function of distance x from the interface. $x < 0$ and $x > 0$ are the CdS and VO_2 areas, respectively. The figures show that the plasmon peaks shift to lower energy after the light is turned on (Fig. 3B). Figure 3C, D show the plasmon peak positions (*i.e.*, the highest peak positions illustrated in Fig. 2B, C) at different coordinates and the corresponding calculation results (*i.e.*, the highest peak positions acquired from the calculated EELS) before and after light exposure. A comparison of Fig. 3C, D shows that both CdS and VO_2 lost electrons (gained holes) upon turning the light on, implied by their plasma peaks shifting to lower energy. The shift of plasma peaks caused only by the inhomogeneous electron density near the CdS/VO_2 interface can be obtained by subtracting the shift caused by the dielectric coupling. This is accomplished by subtracting the red data points from the black data points in Fig. 3C, D. Using Eq. 1, the changes in electron density can be estimated, and the results before and after illumination are shown in blue and orange in Fig. 3E. Figure 3E shows that the change in the electron density near the interface is slightly different for the two data sets,

https://doi.org/10.1038/s41467-025-60243-0

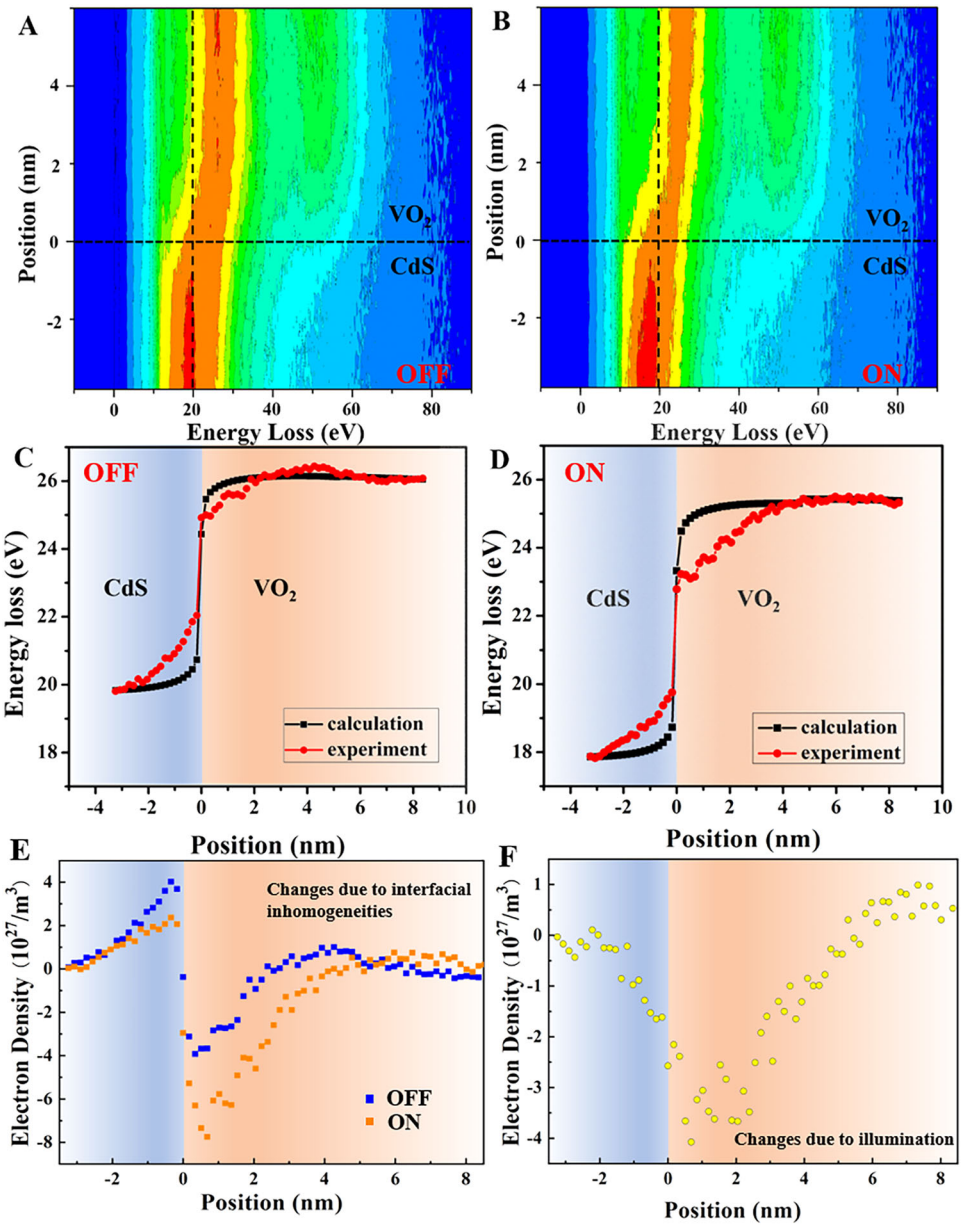

Fig. 3 | The comparison of the valence EELS before and after illumination. **A**, **B** Contour maps of the EELS line scan intensity across the VO_2/CdS interface before and after illumination. The intensity of EELS in the figures decreases from red to blue. Comparing (**A**, **B**), the peak positions shift to lower energy (redshift) in each location after the light exposure. The vertical dashed lines are located at 20 eV and guided to the eyes. **C**, **D** The energy of the highest plasmon peak vs. position coordinate before and after light exposure. The calculation corresponds to the maximum of the peaks computed in Fig. 2E, F. **E** Uneven electron density distributions caused by interfacial inhomogeneity as a function of position. The blue and orange dots are the electron density changes measured before and after light exposure. **F** Differences in electron density changes caused by beam shining (the orange dots (after light exposure) subtract the blue dots (before light exposure) in (**E**), since the interfacial inhomogeneity effects have been removed.

indicating the effect of the illumination on the electron density. This difference obtained by subtracting the blue data points from the orange ones in Fig. 3E is a measure of the changes in electron density caused by illumination as shown in Fig. 3F.

Theoretical calculations

To develop an understanding of the mechanism behind the experimentally observed phenomena in rutile VO_2, density functional theory (DFT) calculations were carried out. Figure 4A illustrates the original band structures of Au/Pt, CdS, and VO_2. The band gap, valence band (E_V), conduction band (E_C), and work function (W) are listed in the figure[45–47]. The work function of rutile VO_2 (4.7 eV) is slightly lower than that of CdS (4.8 eV), thereby facilitating hole doping into the VO_2. The strained rutile VO_2, that results from anchoring to the TiO_2 substrate, is insulator at room temperature, as indicated in Fig. 4A.

We have performed DFT + U calculations to investigate the effect of photodoping on the electronic structure of the strained rutile system by introducing holes in the system. Because the change of electron density is about -4×1027 electron/m^3 (Fig. 3F) at the interfacial area and changes to 0 away from the interface (within 5 nm), we assume an average doping density of -2×1027 electron/m^3, *i.e.*, 2×1027 hole/m^3. The unit cell parameters for rutile VO_2 are a = b = 4.6 Å, c = 2.9 Å, which means each VO_2 has $2 \times 2 \times 10^{27}$ hole/m^3 x $4.6 \times 10^{-10} \times 4.6 \times 10^{-10} \times 2.9 \times 10^{-10}$ m^3 / cell ≈ 0.25 hole/cell. Thus, we adopted 0.25 hole per cell for an order of magnitude calculation. These calculations show that introducing 0.25 holes per VO_2 unit closes the insulating gap, as shown

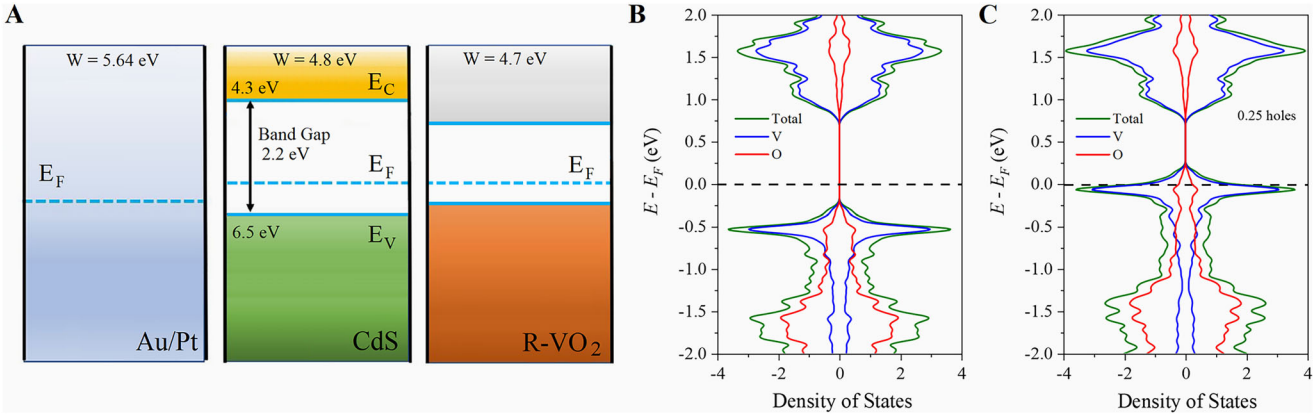

Fig. 4 | Band structures of Au/Pt, CdS, and VO_2. A Schematic diagrams of the Au/Pt, CdS, and R VO_2 band structures. The Fermi energy in each material is indicated by dashed lines. **B** Total (green), O (red), and V (blue) DOS for the VO_2 systems, (**C**) 0.25 holes per formula unit of rutile VO_2. The system with no holes is insulating, whereas the system with 0.25 holes exhibits a metallic behavior.

in Fig. 4B, C. This finding mimics our experiment shown in Fig. 1B, in which illumination of CdS switches the rutile VO_2 from an insulating to a conductive state.

In the unstrained state, rutile VO_2 is a metal, which can be observed from the band structure obtained from the Materials Project (mp-19094). However, when under tensile strain from TiO_2 substrate, our calculations using the same parameters as the Materials Project find that a band gap of 0.6 eV opens up in rutile VO_2. This gap is closed with hole doping. While the DFT + U calculation of hole-doped VO_2 shows metallic behavior, the experimental temperature-resistance curve in Fig. 1B shows semiconducting behavior. The physical scenario that is suggested by our calculations is as follows: At low temperature, no matter the light is on or off, VO_2 is rutile with a relatively big gap and hence holes are uneasy to be injected. The presence of the gap at low temperatures suggests the emergence of an ordered state with our DFT + U calculations, indicating that AFM ordering is the most likely candidate. Moreover, our calculations also suggest that, as the temperature increases reaching the proximity of the ordinary T_{MIT}, the gap may weaken facilitating the hole-injection by the CdS. This process, eventually drives down the transition by 15 K.

Discussion

Though CdS could dope carriers inside of VO_2, its thickness matters. We measured the resistance of several films with different CdS thicknesses as a function of temperature with and without applied light (see Figure S2). We see a strong trend towards higher resistivity in thinner films and a strong reduction in resistivity in the light on state with respect to the light off. The resistivity of the 80 nm film was so high that it could not be conveniently measured without illumination.

The insulating rutile VO_2 has a nominal filling of d^1, thus it should be a Mott insulator. Our experiments and calculations suggest that its MIT through photo doping is a filling-controlled Mott transition. It should be mentioned that, in the current device configuration, we couldn't directly measure the electronic structure of the equilibrium for the hole-doped rutile VO_2. A direct angle-resolved photoemission spectroscopy of a related system, V_2O_3, concluded a different mechanism for the MIT[48]. The MIT in V_2O_3 is caused by a progressive decrease in spectral weight of an itinerant, dispersive quasi particle conduction band without noticeable changes in its dispersion and effective mass. This is accompanied by an energy shift and increase in spectral weight, of a quasi-localized state, which goes from an energy close to the Fermi energy in the metallic state to an energy close to the bottom of the vanishing dispersive band in the insulating state. In our case, the doping is the driving force of the transition.

A more comprehensive measurement of the detailed structure of CdS-capped VO_2 on TiO_2 would be a valuable future study. This would ideally include both electron diffraction, which has excellent sensitivity to small sample volumes, and X-ray diffraction measurements on off-specular Bragg peaks, which has the advantage of macroscopic sampling of the film, along with more straightforward possibilities to model the structure due to the kinematic interaction of X-rays.

In conclusion, a photo-assisted, isostructural doping-driven MIT was found in ultrathin rutile VO_2 film capped with photoactive CdS. The TEM and transport studies together with DFT calculations show that besides the previously reported insulating monoclinic phase, conductive rutile phase, and (meta)stable conductive monoclinic phase, an insulating rutile phase can be stabilized by anchoring between rutile TiO_2 substrate and CdS capping layer. Thus, another missing piece of the puzzle in the VO_2 electronic-crystal structural phase diagram has been found. The tensile strain induced by the substrate puts VO_2 in a new type of stable state, which is the whole idea of hybrid multilayer materials. In contrast, the gradual decay over time of the "on-state" reflects a slow relaxation process rather than a true metastability phenomenon. In addition to the commonly investigated thermal and electric field induced transitions, our results show that heterostructuring a Mott insulator with a photoactive material adds a new degree of freedom. This provides a new way to modulate the MIT, thus widening the applications of VO_2 to photo-active electronic devices. In particular, the isostructural transition reported here shows that VO_2 is a potential material platform for implementing (quasi) nonvolatile, low-energy, fast-response switching devices.

Methods

TEM characterization

A FEI Helios G4 FIB was used for the TEM sample preparation. A JEOL 200CF TEM at Brookhaven National Laboratory was used for the TEM studies. Dual EELS was used, and all EELS spectra were corrected by the zero-loss peaks. For HAADF images, the convergent angle is 21.2 mrad, and the collection angle is between 67 and 275 mrad.

Film growth

An 8 nm thick epitaxial VO_2 film was grown by reactive sputtering on the TiO_2 substrate (oriented along the (001) plane). A 4-mtorr argon/oxygen mixture (8% O_2) was used during deposition, and the substrate was kept at 350 °C during the growth and later cooled down at a rate of 12 °C/min. The CdS, 80 nm thick film was grown on top of the VO_2 using radio frequency magnetron sputtering from a CdS target in a 2

mTorr pure argon atmosphere at 150 °C. Two Au (20 nm) electrodes were patterned on the CdS/VO_2 heterostructure films. Room temperature XRD measurements were done in a Rigaku SmartLab system. Single-phase growth was confirmed by XRD, textured along ⟨002⟩ for VO_2 and H⟨002⟩ for CdS. Transport measurements were carried out on a Montana C2 S50 Cryocooler and TTPX Lakeshore cryogenic probe station, using a Keithley 6221 current source and a Keithley 2182 A nanovoltmeter.

Solar light generator

The simulated solar light is provided by a 150 W solar simulator equipped with an air mass 1.5 global (AM 1.5 G) filter (Newport), and the light power was calibrated to 1 Sun (100 mW/cm^2) using a quartz-windowed Si solar cell (Newport).

Data availability

The authors declare that the data supporting the findings of this study are available within the paper and its supplementary information file. Source data are provided with this paper.

References

1. Marković, D., Mizrahi, A., Querlioz, D. & Grollier, J. Physics for neuromorphic computing. *Nat. Rev. Phys.* **2**, 499–510 (2020).
2. Valle, J. D. et al. Spatiotemporal characterization of the field-induced insulator-to-metal transition. *Science* **373**, 907–911 (2021).
3. Wang, Z. et al. Resistive switching materials for information processing. *Nat. Rev. Mater.* **5**, 173–195 (2020).
4. Rocco, R. et al. Exponential Escape Rate of Filamentary Incubation in Mott Spiking Neurons. *Phys. Rev. Appl.* **17**, 024028 (2022).
5. Valle, J. D., Ramírez, J. G., Rozenberg, M. J. & Schuller, I. K. Challenges in materials and devices for resistive-switching-based neuromorphic computing. *J. Appl. Phys.* **124**, 211101 (2018).
6. Qiu, E. et al. Stochasticity in the synchronization of strongly coupled spiking oscillators. *Appl. Phys. Lett.* **122**, 094105 (2023).
7. Qiu, E. et al. Stochastic transition in synchronized spiking nanooscillators. *Proc. Natl Acad. Sci.* **120**, e2303765120 (2023).
8. Shabalin, A. G. et al. Nanoscale Imaging and Control of Volatile and Non-Volatile Resistive Switching in VO_2. *Small* **16**, 2005439 (2020).
9. Wang, S. et al. Ultrafast photo-induced dynamics across the metal-insulator transition of VO_2. *Europhys. Lett.* **118**, 27005 (2017).
10. Butakov, N. A. et al. Broadband Electrically Tunable Dielectric Resonators Using Metal–Insulator Transitions. *ACS Photonics* **5**, 4056–4060 (2018).
11. Dietze, S. H. et al. X-ray-induced persistent photoconductivity in vanadium dioxide. *Phys. Rev. B* **90**, 165109 (2014).
12. Li, J. et al. Laser-induced selective local patterning of vanadium oxide phases. *Adv. Compos. Hybrid. Mater.* **8**, 157 (2025).
13. Morin, F. J. Oxides Which Show a Metal-to-Insulator Transition at the Neel Temperature. *Phys. Rev. Lett.* **3**, 34–36 (1959).
14. Luo, R. et al. Spin Seebeck effect at low temperatures in the nominally paramagnetic insulating state of vanadium dioxide. *Appl. Phys. Lett.* **121**, 102404 (2022).
15. Morrison, V. R. et al. A photoinduced metal-like phase of monoclinic VO_2 revealed by ultrafast electron diffraction. *Science* **346**, 445–448 (2014).
16. Wegkamp, D. et al. Instantaneous Band Gap Collapse in Photoexcited Monoclinic VO_2 due to Photocarrier Doping. *Phys. Rev. Lett.* **113**, 216401 (2014).
17. Lee, D. et al. Isostructural metal-insulator transition in VO_2. *Science* **362**, 1037–1040 (2018).
18. Mondal, D. et al. Modulation-doping a correlated electron insulator. *Nat. Commun.* **14**, 6210 (2023).
19. Kalsi, T., Mitra, H., Roy, T. K., Godara, S. K. & Kumar, P. Comprehensive Analysis of Band Gap and Nanotwinning in Cd1–xMgxS QDs. *Cryst. Growth Des.* **20**, 6699–6706 (2020).
20. Navarro, H. et al. A hybrid optoelectronic Mott insulator. *Appl. Phys. Lett.* **118**, 141901 (2021).
21. Adda, C. et al. An optoelectronic heterostructure for neuromorphic computing: CdS/V_3O_5. *Appl. Phys. Lett.* **121**, 041901 (2022).
22. Cheng, L., Xiang, Q., Liao, Y. & Zhang, H. CdS-Based photocatalysts. *Energy Environ. Sci.* **11**, 1362–1391 (2018).
23. Navarro, H. et al. Light-Induced Decoupling of Electronic and Magnetic Properties in Manganites. *Phys. Rev. Appl.* **19**, 044077 (2023).
24. Navarro, H. et al. Disentangling transport mechanisms in a correlated oxide by photoinduced charge injection. *Phys. Rev. Mater.* **7**, L123201 (2023).
25. Cheng, S. et al. Operando characterization of conductive filaments during resistive switching in Mott VO2. *Proc. Natl Acad. Sci.* **118**, e2013676118 (2021).
26. Cheng, S. et al. Inherent stochasticity during insulator-metal transition in VO_2. *Proc. Natl Acad. Sci.* **118**, e2105895118 (2021).
27. Park, J. et al. Direct Quantification of Heat Generation Due to Inelastic Scattering of Electrons Using a Nanocalorimeter. *Adv. Sci.* **8**, 2002876 (2021).
28. Shiga, D. et al. Thickness dependence of electronic structures in VO_2 ultrathin films: Suppression of the cooperative Mott-Peierls transition. *Phys. Rev. B* **102**, 115114 (2020).
29. Yang, M. et al. Suppression of Structural Phase Transition in VO_2 by Epitaxial Strain in Vicinity of Metal-insulator Transition. *Sci. Rep.* **6**, 23119 (2016).
30. Fan, L. L. et al. Strain Dynamics of Ultrathin VO2 Film Grown on TiO_2 (001) and the Associated Phase Transition Modulation. *Nano Lett.* **14**, 4036–4043 (2014).
31. Mecklenburg, M. et al. Nanoscale temperature mapping in operating microelectronic devices. *Science* **347**, 629–632 (2015).
32. Rez, P. & Muller, D. A. The Theory and Interpretation of Electron Energy Loss Near-Edge Fine Structure. *Annu. Rev. Mater. Res.* **38**, 535–558 (2008).
33. Pines, D. Elementary Excitations in Solids. (W.A. Benjamin, New York; 1963).
34. Reed, B. W., Chen, J. M., MacDonald, N. C., Silcox, J. & Bertsch, G. F. Fabrication and STEM/EELS measurements of nanometer-scale silicon tips and filaments. *Phys. Rev. B* **60**, 5641–5652 (1999).
35. Meng, Q. et al. Quantification of Charge Transfer at the Interfaces of Oxide Thin Films. *J. Phys. Chem. A* **123**, 4632–4637 (2019).
36. Moreau, P., Brun, N., Walsh, C. A., Colliex, C. & Howie, A. Relativistic effects in electron-energy-loss-spectroscopy observations of the Si/SiO_2 interface plasmon peak. *Phys. Rev. B* **56**, 6774–6781 (1997).
37. Garcia-Molina, R., Gras-Marti, A., Howie, A. & Ritchie, R. H. Retardation effects in the interaction of charged particle beams with bounded condensed media. *J. Phys. C: Solid State Phys.* **18**, 5335–5345 (1985).
38. Bolton, J. P. R. & Chen, M. Electron energy loss in multilayered slabs. *Ultramicroscopy* **60**, 247–263 (1995).
39. Aruta, C. et al. Orbital occupation, atomic moments, and magnetic ordering at interfaces of manganite thin films. *Phys. Rev. B* **80**, 014431 (2009).
40. Pinta, C. et al. Suppression of spin-state transition in epitaxially strained $LaCoO_3$. *Phys. Rev. B* **78**, 174402 (2008).
41. Merwe, J. H. v.d. On the Stresses and Energies associated with Inter-Crystalline Boundaries. *Proc. Phys. Soc. Sect. A* **63**, 616–637 (1950).
42. Meng, Q., Wu, L. & Zhu, Y. Phonon scattering of interfacial strain field between dissimilar lattices. *Phys. Rev. B* **87**, 064102 (2013).
43. Nakagawa, N., Hwang, H. Y. & Muller, D. A. Why some interfaces cannot be sharp. *Nat. Mater.* **5**, 204–209 (2006).
44. Vaz, C. A. F. et al. Origin of the Magnetoelectric Coupling Effect in Pb(Zr0.2Ti0.8)O3 / La0.8Sr0.2MnO3 Multiferroic Heterostructures. *Phys. Rev. Lett.* **104**, 127202 (2010).

45. Ngo, T. D. et al. Fermi-Level Pinning Free High-Performance 2D CMOS Inverter Fabricated with Van Der Waals Bottom Contacts. *Adv. Electron. Mater.* **7**, 2001212 (2021).
46. Heo, J. et al. Clean thermal decomposition of tertiary-alkyl metal thiolates to metal sulfides: environmentally-benign, non-polar inks for solution-processed chalcopyrite solar cells. *Sci. Rep.* **6**, 36608 (2016).
47. Sohn, A. et al. Evolution of local work function in epitaxial VO_2 thin films spanning the metal-insulator transition. *Appl. Phys. Lett.* **101**, 191605 (2012).
48. Thees, M. et al. Imaging the itinerant-to-localized transmutation of electrons across the metal-to-insulator transition in V_2O_3. *Sci. Adv.* **7**, eabj1164 (2021).

Acknowledgements

We would like to acknowledge Tianxing D. Wang and Juan A. Hofer from University of California San Diego (UCSD) for the help with XRD measurements. The structural characterization, transport, TEM and collaboration between Brookhaven National Laboratory (BNL), CNRS and the UCSD were supported through an Energy Frontier Research Center program funded by the US Department of Energy (DOE), Office of Science, Basic Energy Sciences, under Grant DE-SC0019273. Electron microscopy work at BNL and the use of BNL's Center for Functional Nanomaterials were supported by DOE-BES, the Division of Materials Science and Engineering, and the Division of Science User Facility, respectively, under Contract no. DE-SC0012704.

Author contributions

T.E.M. studies: S.B.C., X.L., A.P.; Thin film growth: H.N.; Theoretical calculations: Z.W., J.K., Q.M., C.C., M.R., S.P.O.; Methodology: S.B.C., H.N., C.Z., M.L., A.C.B., M.P.M.D.; Supervision: I.K.S., Y.Z.; Writing—Original draft: S.B.C., H.N., Z.W.; Writing—review &editing: M.R., I.K.S., Y.Z.

Competing interests

The authors declare no competing interests.

Additional information

Supplementary information The online version contains supplementary material available at https://doi.org/10.1038/s41467-025-60243-0.

Correspondence and requests for materials should be addressed to Yimei Zhu.

Peer review information *Nature Communications* thanks Teruo Kanki, and the other, anonymous, reviewers for their contribution to the peer review of this work. A peer review file is available.